

Turbulent Dynamo Action in Binary Neutron Star Mergers

Eduardo M. Gutiérrez,^{1,2} David Radice,^{1,2,3} Jacob Fields,⁴ and James M. Stone⁴

¹*Institute for Gravitation and the Cosmos,*

The Pennsylvania State University, University Park, PA 16802, USA

²*Department of Physics, The Pennsylvania State*

University, University Park, PA 16802, USA

³*Department of Astronomy & Astrophysics,*

The Pennsylvania State University, University Park, PA 16802, USA

⁴*Institute for Advanced Study, Princeton, NJ 08540, USA*

Abstract

Binary neutron star mergers are expected to generate intense magnetic fields that power relativistic and non-relativistic outflows and shape their multimessenger signatures. These fields likely arise from the turbulent amplification of initially weak magnetic fields during the merger, particularly via the Kelvin–Helmholtz instability at the collisional interface between the stars. While previous studies have shown efficient amplification to magnetar-level strengths, the degree of large-scale coherence of the resulting field remains uncertain. We present general-relativistic, dynamical spacetime, magnetohydrodynamic simulations following the evolution of initially weak, pulsar-like magnetic fields in a binary neutron star merger. We find rapid magnetic field growth at small scales with clear signatures of small-scale turbulent dynamo action. At the highest resolutions, we additionally observe the emergence of coherent magnetic structures on larger scales. Our results imply that strong, ordered magnetic fields may be present immediately after merger, with important implications for the subsequent evolution of the remnant and its observable electromagnetic and gravitational-wave signals.

Binary neutron star (NS) systems merge at the end of a $\sim 10-10^4$ Myr gravitational wave (GW) driven inspiral [1]. This timescale is comparable to, or potentially larger than, the inferred decay time for pulsar magnetic fields [2, 3]. As such, the NSs are not expected to be strongly magnetized at the time of merger. However, strong, ordered magnetic fields are necessary to produce relativistic outflows matching the energies inferred from gamma-ray bursts. This is exemplified by GW170817, the first NS merger to be observed in both gravitational- and electromagnetic waves. This system is inferred to have merged $\gtrsim 1$ Gyr after the birth of the second NS [4, 5], but nevertheless produced a strong relativistic jet that was observed slightly off-axis [6, 7]. The presence of strong electromagnetic fields also provides a natural explanation for the UV/optical light curves on the first day of the merger, the so-called blue kilonova [8–10]. Turbulence during the merger must have amplified the initial magnetic field, but the details of this process are far from understood [11].

In a seminal paper, Price and Rosswog [12] first demonstrated, with Newtonian smooth particle hydrodynamics simulations, that the Kelvin–Helmholtz instability (KHI) in the shear layer formed when the stars first come into contact can strongly amplify the initial magnetic field of the binary. These results were later confirmed by both local and global grid-based simulations with adaptive mesh refinement [13–18]. However, to power collimated outflows, the magnetic field in the remnant does not only need to be strong, but also coherent at large scales [19]. Tangled magnetic fields produced by the KHI are expected to undergo a reverse cascade and produce large-scale fields on a timescale of the order of the Alfvén time $t_A \gtrsim 1$ second. Numerical evidence that this phenomenon takes place after merger has been reported by Aguilera-Miret and collaborators on the basis of large-eddy simulations with subgrid models [20, 21]. However, this process is too slow to play a dynamical role before black hole formation for most systems. In a parallel line of investigation, Kiuchi and collaborators have shown that large-scale fields, if they exist in the first place, can be self-consistently supported by dynamo action in the shear layers of the remnant after merger [22]. Their work, as well as most of the literature, considers binaries that already have strong ordered fields before merger in anticipation of the fact that such fields will be generated by the KHI [10, 23]. However, the ability of the KHI to create the required large-scale magnetic flux in the few milliseconds it operates has not been previously demonstrated. In this work, we present strong positive evidence supporting this idea.

We perform general-relativistic magnetohydrodynamics (MHD) simulations of an equal

mass ($M_1 = M_2 = 1.3 M_{\odot}$) binary NS system merging at the end of a gravitational-wave driven inspiral. We initialize the magnetic field assuming each star has a purely dipolar field, with the dipole aligned with the binary angular momentum vector. The maximum field, achieved at the center of the stars, is $\simeq 2 \times 10^{12}$ G, corresponding to a realistic maximum surface field of $\simeq 3 \times 10^{10}$ G. As discussed in more detail in the Supplementary Materials, we first perform a global, adaptive mesh refinement simulation of the binary, with maximum resolution of $2^{-4} GM_{\odot}/c^2 \simeq 92$ m. Then, we follow this up with a set of “zoom-in” simulations, achieving much higher resolution. The zoom-in simulations consider a cubical region $[-L, L]^3$ of side length $2L$, with $L = 4 GM_{\odot}/c^2 \simeq 5.91$ km centered at the (Newtonian) center of mass of the system. Initial and boundary data, as well as the time-dependent background spacetime geometry, are obtained from the global NS merger simulation.

This mapping allowed us to achieve unprecedented grid resolutions of down to $\Delta x = 2^{-9} GM_{\odot}/c^2 \simeq 2.9$ m. Simulations with $\Delta x = 2^{-\ell} GM_{\odot}/c^2$ for $\ell = 4, 5, 6, 7, 8$ are carried out in an unigrid setup, while the highest resolution calculation uses a mesh refinement grid with $\Delta x = 2^{-9} GM_{\odot}/c^2$ in the inner $[-L/4, L/4]^3$, which contains the most intense vortical structures, and by a factor of two in the surrounding region $[-L/2, L/2]^3$ and four in the remainder of the grid (outer layers). The combination of unigrid and mesh-refinement calculations allows us to quantify the importance of the non-local nonlinear dynamics. Our simulations do not include explicit viscosity or resistivity; however, the width of the shear layer is limited by the scale height on the surface of the NSs ($\rho/\partial_r \rho$), which is of the order of 50 m. In other words, gravity introduces a length scale in this system, so the flow is not expected to exhibit self-similar behavior to arbitrarily small scales.

The qualitative dynamics of the simulation, and our workflow, are summarized in Fig. 1. At the time of merger, the binary develops a very hot shear layer with a velocity jump of $\Delta v \approx 0.3c$. This layer rapidly generates vortical structures where the field undergoes exponential amplification. Initially, such amplification is confined to a narrow region at the interface between the stars. At ≈ 1.5 ms, the shear layer grows in size as vortices produced by the primary KHI themselves become KH-unstable (panel (b)). Within approximately one rotational period $\tau \sim 1$ ms, all the initial unstable vortices have merged, and a large fraction of the box volume is filled with turbulent, vortical structures with a strongly amplified field (panel (c)). The turbulent layer is not confined to the equatorial plane but also extends vertically, as shown in the lower-right panel, which displays a 3D rendering of the magnetic

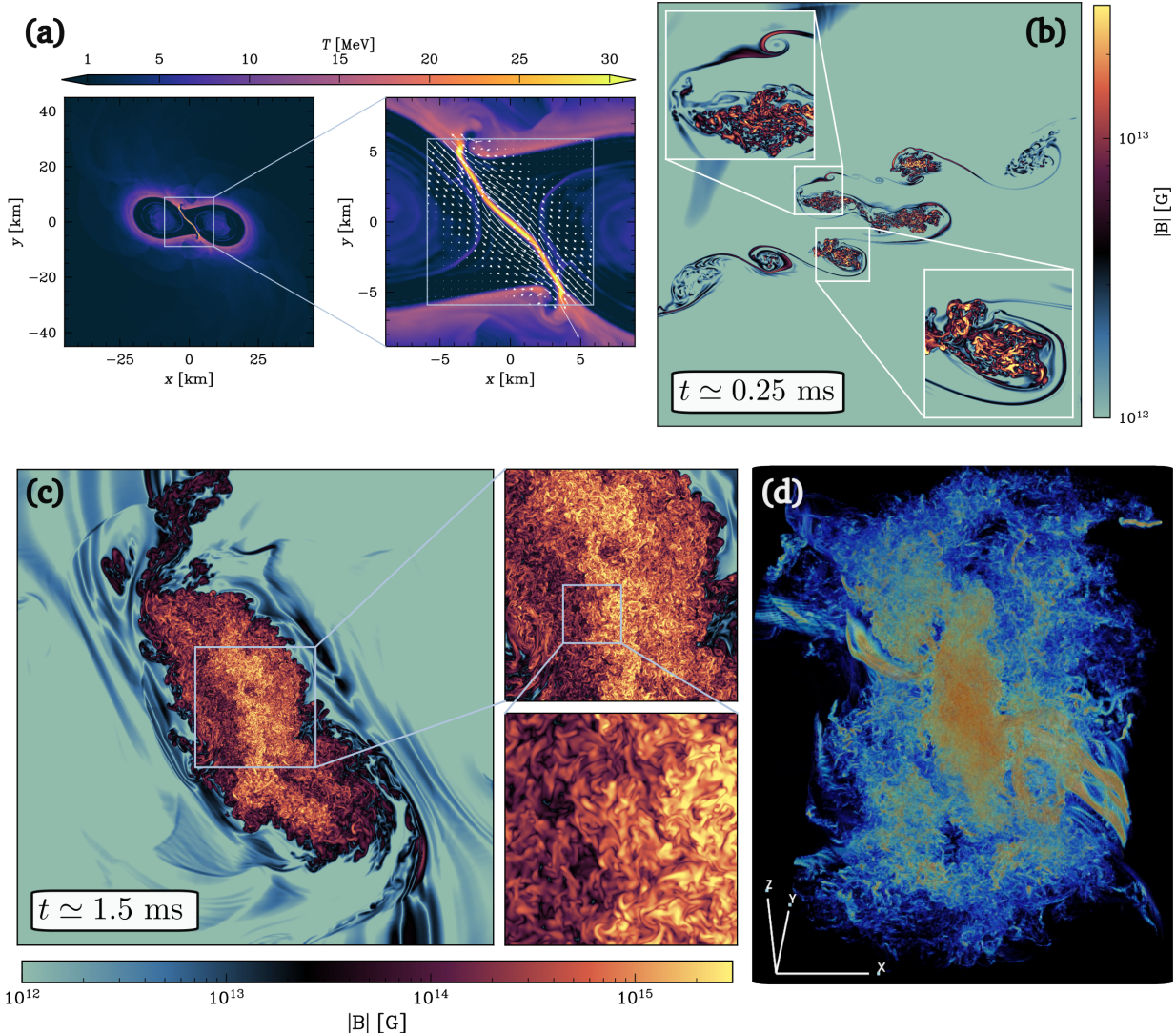


FIG. 1. **Turbulent magnetic-field amplification in the merger shear layer.** (a) Equatorial snapshot of temperature at the time of hand-off; the right subpanel shows a zoom-in of the hot shear layer region with the arrows representing the velocity vector field in the co-rotating frame. The white box on the right subplot shows the box used in the zoom-in simulation. (b) Magnetic field strength at $t \simeq 0.25$ ms in the zoom-in simulation. The shear layer has rotated approximately 90° and vortices of different sizes have already formed along it due to the development of the KHI; in these vortices, the magnetic field is amplified. (c) Magnetic field strength at $t \simeq 1.5$ ms. The vortices have merged, and turbulence is fully developed in a thick rotating layer. Note that the upper limit for the magnetic field colormap is higher than in (b). (d) Three-dimensional rendering of the magnetic field strength at $t \approx 0.6$ ms, showing the global structure of the field.

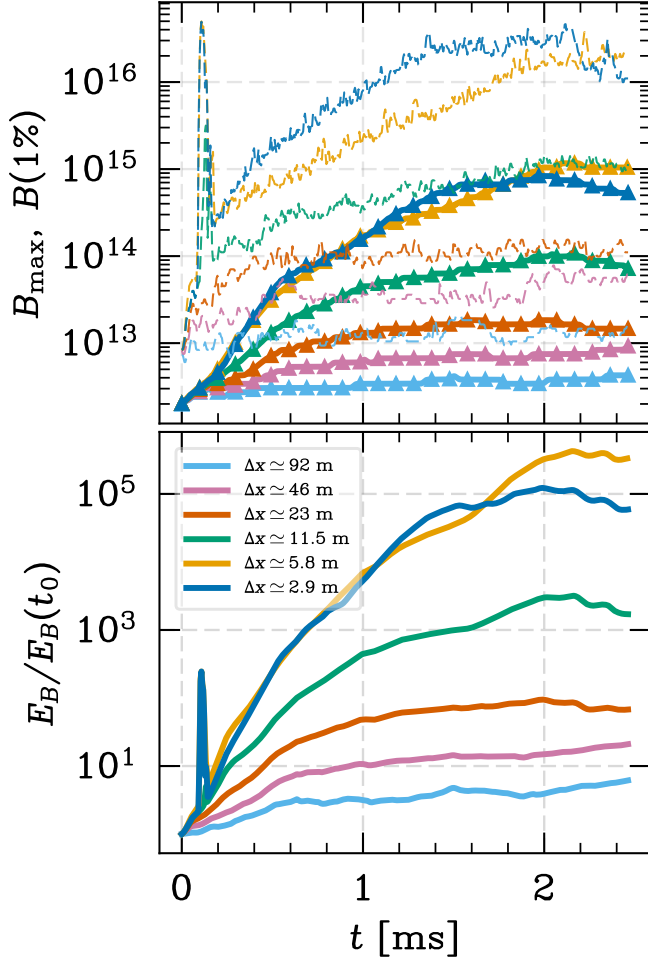


FIG. 2. **Magnetic field amplification in the early post-merger phase.** *Upper panel:* 99th mass-weighted percentile of the magnetic field strength (thick lines with triangular markers), meaning that only 1% of the mass of the fluid mass attains larger values, together with the maximum field strength (dashed lines). *Lower panel:* Time evolution of the total magnetic energy within the simulation domain, normalized to its initial value.

field strength.

Magnetic field amplification is highly intermittent: the field is tightly wound up in small-scale turbulent eddies, where it is locally amplified by orders of magnitude—reaching strengths of \sim few $\times 10^{16}$ G—before undergoing turbulent reconnection (see Fig. 2). This degree of intermittency can be quantified in terms of the cumulative distribution function for the magnetic field, which we find to form a clear power-law tail $p(B > B_0) \sim B_0^{-p}$ with $p \lesssim 0.2$ (see Supplemental material).

The total magnetic field energy (Fig. 2) saturates within ~ 2 ms, a timescale that is comparable to the rotational frequency of the system. This is long compared to the eddy turnover timescale of the region we are considering, $\tau_E \sim L/(0.1c) \simeq 0.2$ ms, or the even shorter eddy turnover time for the vortical structures seeded by the KHI. The “slow” saturation of the magnetic energy of the remnant is the result of two factors. First, the field achieves a critical balance between turbulent amplification and reconnection in the core of the most intense vortical structures (Fig. 2). This balance depends on the grid resolution employed in the simulations because of the lack of explicit resistivity in the simulations. Second, it is the growth in size of the turbulent region that controls the overall energy budget for the remnant. This interplay of very small and large-scale dynamics is a hallmark of MHD turbulence. Our simulations achieve convergence in global, integrated quantities at resolutions finer than ~ 5.8 m, when the scale-height at the surface of the stars, which sets the width of the shear-layer, is fully resolved. This can be seen from the value of the 99th percentile of the field in Fig. 2, as well as in the energy spectra discussed below. The overall magnetic energy starts to deviate between the two highest resolution simulations at late times, when the turbulent region spreads outside the most resolved portion of the grid in the $\Delta x \simeq 2.9$ m resolution run. In contrast, for pointwise magnetic field values, we cannot exclude the possibility that even stronger fields occur in nature on smaller, unresolved scales.

We investigate the nature of turbulence in our simulations by calculating the power spectra for the density-weighted Eulerian-frame velocity $\sqrt{\rho} \mathbf{v}$ and magnetic field \mathbf{B} , shown in Figs. 3 and 4. Both velocity and magnetic spectra are fully developed after approximately one turnover time. The velocity power spectrum shows a clear Kolmogorov $k^{-5/3}$ scaling for $k \gtrsim 10$, indicative of a fully developed rotational flow. The kinetic inertial range extends over more than a decade in k space in the highest resolution simulations. The magnetic energy spectrum quickly develops an extended region with power-law behavior with scaling k^p , with $p \simeq 0.75$, somewhat shallower than $k^{3/2}$ expected in a Kazantsev turbulent dynamo. The spectrum peaks at increasingly small scales for higher resolution simulations, implying that the structure of the field is increasingly more tangled as the turbulence is better resolved. Equipartition between magnetic and kinetic energy is not achieved in our simulations (see Supplemental material). At later times, in the highest resolution simulations, the dynamics change qualitatively, and the magnetic field grows at large scales. This is reflected by the steepening of the magnetic spectrum to $k^{3/2}$ and its growth at the largest scales. The fact

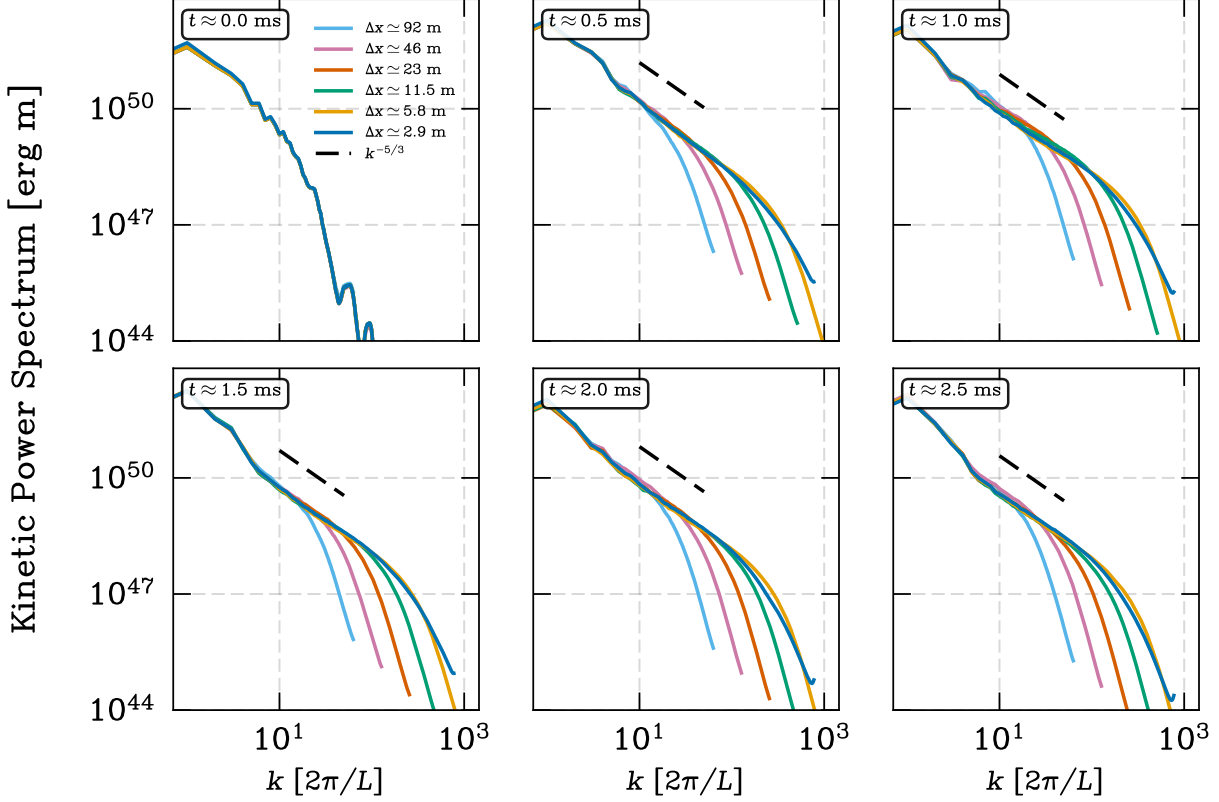


FIG. 3. **Kinetic energy power spectra at selected times for the six simulations.** The short black dashed line shows the Kolmogorov scaling $\sim k^{-5/3}$; times and numerical resolutions are indicated in the in-panel labels.

that this growth is only seen in the highest resolution simulations, and not at in the lower resolution calculations, which use the same initial and boundary conditions, demonstrates that the growth at large scale in the field is not due to the large-scale dynamics of the system (e.g., due to the advection of magnetic flux into the simulation volume), but rather the result of the intrinsic non-linear turbulent dynamics.

Our simulations show that the KHI in the context of binary NS mergers can operate as a turbulent dynamo, creating large-scale, magnetar-level fields within milliseconds of the stars coming into contact. The field strengths achieved in our simulations are large enough to leave an imprint in the post-merger gravitational-wave signal from these binaries [24, 25], whose measurement is a key science goal for next-generation ground-based detectors such as the NEMO [26], the Einstein Telescope [27], and Cosmic Explorer [28]. If these intense, large-scale fields were to break out of the remnant surface, they could also power gamma-ray flares

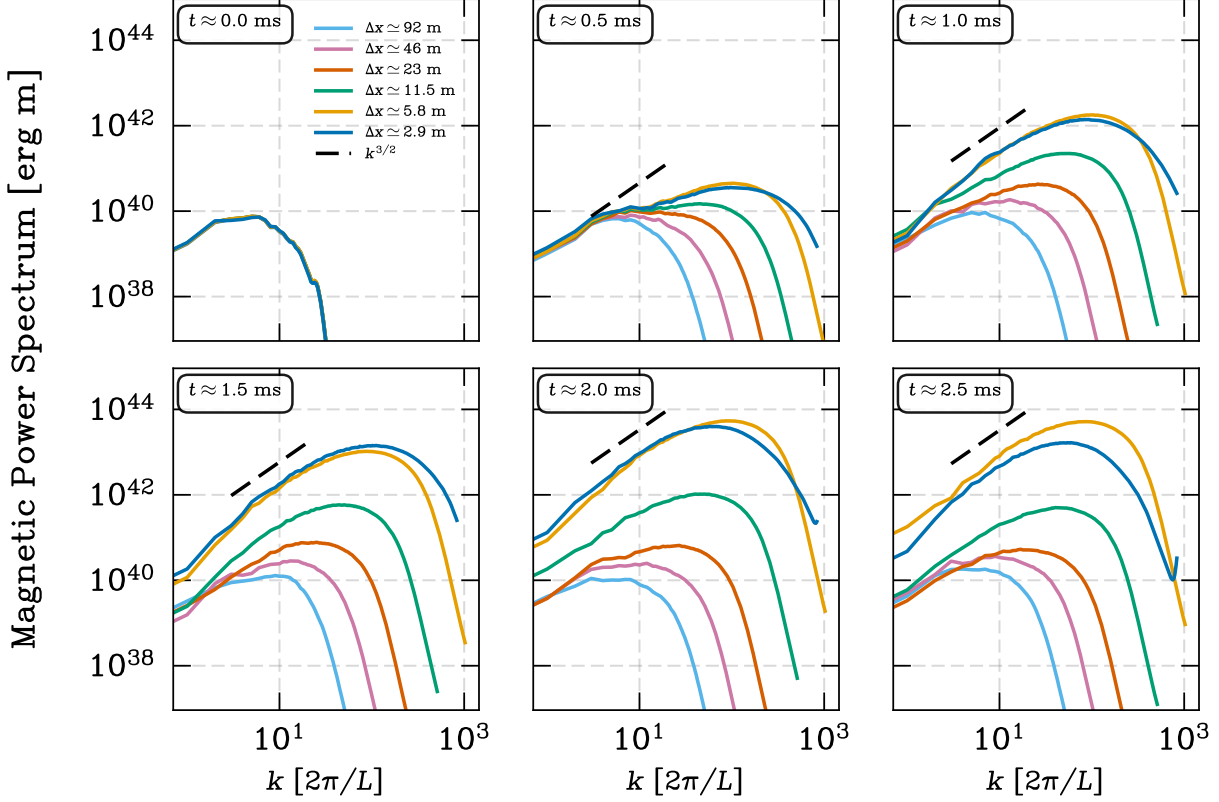


FIG. 4. **Magnetic energy spectra at selected times for the six simulations.** The short black dashed line shows the Kazantsev scaling $\sim k^{3/2}$; times and numerical resolutions are indicated in the in-panel labels.

[29] and explain recently discovered quasi-periodic oscillations (QPOs) in some short gamma-ray bursts [30]. These QPOs have been interpreted as oscillation modes of the remnant [31]; however, within the standard paradigm for neutron-star merger dynamics, such oscillations are expected to be rapidly damped by gravitational-wave radiation reaction [32, 33]. At the same time, it remains unclear whether the magnetic-field strengths achieved in our simulations would be sufficient to undergo buoyant breakout, and additional amplification may be required for this mechanism to operate.

Our results imply that strong, large-scale magnetic fields are present immediately after the merger. These have the potential to launch relativistic jets before the oscillation modes of the remnant have been completely damped. These fields can also be expected to centrifugally accelerate the merger debris to trans-relativistic velocities, which would produce an UV/optical flash minutes to hours after merger [8, 10], whose presence could be tested

with future observations.

Acknowledgements EG and DR were supported by the National Science Foundation under Grant PHY-2407681. DR also acknowledges support from the Sloan Foundation, from the Department of Energy, Office of Science, Division of Nuclear Physics under Award Number DE-SC0024388, from the National Science Foundation under Grants No. PHY-2020275, PHY-2116686, and PHY-2512802. DR, JF, and JS acknowledge support from the National Aeronautics and Space Administration under Grant No. 80NSSC25K213. Zoom-in simulations were performed on Aurora at the Argonne Leadership Computing Facility, which is a DOE Office of Science User Facility supported under Contract DE-AC02-06CH11357. An award of computer time was provided by the INCITE program. Global simulations were performed on Perlmutter, at the National Energy Research Scientific Computing Center (NERSC), a Department of Energy User Facility using NERSC award ERCAP0031370.

- [1] K. A. Postnov and L. R. Yungelson, The Evolution of Compact Binary Star Systems, *Living Rev. Rel.* **17**, 3 (2014), arXiv:1403.4754 [astro-ph.HE].
- [2] P. Goldreich and A. Reisenegger, Magnetic Field Decay in Isolated Neutron Stars, *Astrophys. J.* **395**, 250 (1992).
- [3] J. A. Pons and D. Viganò, Magnetic, thermal and rotational evolution of isolated neutron stars, *Liv. Rev. Comput. Astrophys.* **5**, 3 (2019), arXiv:1911.03095 [astro-ph.HE].
- [4] B. P. Abbott *et al.* (LIGO Scientific, Virgo), On the Progenitor of Binary Neutron Star Merger GW170817, *Astrophys. J. Lett.* **850**, L40 (2017), arXiv:1710.05838 [astro-ph.HE].
- [5] A. J. Levan *et al.*, The environment of the binary neutron star merger GW170817, *Astrophys. J. Lett.* **848**, L28 (2017), arXiv:1710.05444 [astro-ph.HE].
- [6] G. Ghirlanda *et al.*, Compact radio emission indicates a structured jet was produced by a binary neutron star merger, *Science* **363**, 968 (2019), arXiv:1808.00469 [astro-ph.HE].
- [7] K. P. Mooley, A. T. Deller, O. Gottlieb, E. Nakar, G. Hallinan, S. Bourke, D. A. Frail, A. Horesh, A. Corsi, and K. Hotokezaka, Superluminal motion of a relativistic jet in the neutron-star merger GW170817, *Nature* **561**, 355 (2018), arXiv:1806.09693 [astro-ph.HE].
- [8] B. D. Metzger, T. A. Thompson, and E. Quataert, A magnetar origin for the kilonova ejecta

- in GW170817, *Astrophys. J.* **856**, 101 (2018), arXiv:1801.04286 [astro-ph.HE].
- [9] P. Mösta, D. Radice, R. Haas, E. Schnetter, and S. Bernuzzi, A magnetar engine for short GRBs and kilonovae, *Astrophys. J. Lett.* **901**, L37 (2020), arXiv:2003.06043 [astro-ph.HE].
- [10] L. Combi and D. M. Siegel, Jets from Neutron-Star Merger Remnants and Massive Blue Kilonovae, *Phys. Rev. Lett.* **131**, 231402 (2023), arXiv:2303.12284 [astro-ph.HE].
- [11] D. Radice and I. Hawke, Turbulence modelling in neutron star merger simulations, *Liv. Rev. Comput. Astrophys.* **10**, 1 (2024), arXiv:2402.03224 [astro-ph.HE].
- [12] D. Price and S. Rosswog, Producing ultra-strong magnetic fields in neutron star mergers, *Science* **312**, 719 (2006), arXiv:astro-ph/0603845.
- [13] M. Obergaulinger, M. A. Aloy, and E. Muller, Local simulations of the magnetized Kelvin-Helmholtz instability in neutron-star mergers, *Astron. Astrophys.* **515**, A30 (2010), arXiv:1003.6031 [astro-ph.SR].
- [14] J. Zrake and A. I. MacFadyen, Magnetic energy production by turbulence in binary neutron star mergers, *Astrophys. J. Lett.* **769**, L29 (2013), arXiv:1303.1450 [astro-ph.HE].
- [15] B. Giacomazzo, J. Zrake, P. Duffell, A. I. MacFadyen, and R. Perna, Producing Magnetar Magnetic Fields in the Merger of Binary Neutron Stars, *Astrophys. J.* **809**, 39 (2015), arXiv:1410.0013 [astro-ph.HE].
- [16] K. Kiuchi, K. Kyutoku, Y. Sekiguchi, M. Shibata, and T. Wada, High resolution numerical-relativity simulations for the merger of binary magnetized neutron stars, *Phys. Rev. D* **90**, 041502 (2014), arXiv:1407.2660 [astro-ph.HE].
- [17] K. Kiuchi, P. Cerdá-Durán, K. Kyutoku, Y. Sekiguchi, and M. Shibata, Efficient magnetic-field amplification due to the Kelvin-Helmholtz instability in binary neutron star mergers, *Phys. Rev. D* **92**, 124034 (2015), arXiv:1509.09205 [astro-ph.HE].
- [18] M. Chabanov, S. D. Tootle, E. R. Most, and L. Rezzolla, Crustal Magnetic Fields Do Not Lead to Large Magnetic-field Amplifications in Binary Neutron Star Mergers, *Astrophys. J. Lett.* **945**, L14 (2023), arXiv:2211.13661 [astro-ph.HE].
- [19] R. Narayan, I. V. Igumenshchev, and M. A. Abramowicz, Magnetically arrested disk: an energetically efficient accretion flow, *Publ. Astron. Soc. Jap.* **55**, L69 (2003), arXiv:astro-ph/0305029.
- [20] R. Aguilera-Miret, C. Palenzuela, F. Carrasco, and D. Viganò, Role of turbulence and winding in the development of large-scale, strong magnetic fields in long-lived remnants of binary

- neutron star mergers, [Phys. Rev. D](#) **108**, 103001 (2023), arXiv:2307.04837 [astro-ph.HE].
- [21] R. Aguilera-Miret, J.-E. Christian, S. Rosswog, and C. Palenzuela, Robustness of Magnetic Field Amplification in Neutron Star Mergers, [Mon. Not. Roy. Astron. Soc.](#) **3067**, 3077 (2025), arXiv:2504.10604 [astro-ph.HE].
- [22] K. Kiuchi, A. Reboul-Salze, M. Shibata, and Y. Sekiguchi, A large-scale magnetic field produced by a solar-like dynamo in binary neutron star mergers, [Nature Astron.](#) **8**, 298 (2024), arXiv:2306.15721 [astro-ph.HE].
- [23] C. Musolino, L. Rezzolla, and E. R. Most, On the Impact of Neutrinos on the Launching of Relativistic Jets from “Magnetars” Produced in Neutron Star Mergers, [Astrophys. J. Lett.](#) **984**, L61 (2025), arXiv:2410.06253 [astro-ph.HE].
- [24] A. Tsokaros, J. Bamber, M. Ruiz, and S. L. Shapiro, Masking the Equation-of-State Effects in Binary Neutron Star Mergers, [Phys. Rev. Lett.](#) **134**, 121401 (2025), arXiv:2411.00939 [gr-qc].
- [25] I. Rainho, J. Bamber, D. Guerra, M. Miravet-Tenés, M. Ruiz, A. Tsokaros, and S. L. Shapiro, Impact of Magnetic Field Topology on Electromagnetic and Gravitational Waves from Binary Neutron Star Merger Remnants, (2025), arXiv:2510.17511 [astro-ph.HE].
- [26] K. Ackley *et al.*, Neutron Star Extreme Matter Observatory: A kilohertz-band gravitational-wave detector in the global network, [Publ. Astron. Soc. Austral.](#) **37**, e047 (2020), arXiv:2007.03128 [astro-ph.HE].
- [27] M. Punturo *et al.*, The Einstein Telescope: A third-generation gravitational wave observatory, [Class. Quant. Grav.](#) **27**, 194002 (2010).
- [28] D. Reitze *et al.*, Cosmic Explorer: The U.S. Contribution to Gravitational-Wave Astronomy beyond LIGO, [Bull. Am. Astron. Soc.](#) **51**, 035 (2019), arXiv:1907.04833 [astro-ph.IM].
- [29] E. R. Most and E. Quataert, Flares, Jets, and Quasiperiodic Outbursts from Neutron Star Merger Remnants, [Astrophys. J. Lett.](#) **947**, L15 (2023), arXiv:2303.08062 [astro-ph.HE].
- [30] C. Chirenti, S. Dichiara, A. Lien, M. C. Miller, and R. Preece, Kilohertz quasiperiodic oscillations in short gamma-ray bursts, [Nature](#) **613**, 253 (2023), arXiv:2301.02864 [astro-ph.HE].
- [31] V. Guedes, D. Radice, C. Chirenti, and K. Yagi, Tight Bound on the Neutron Star Radius with Quasiperiodic Oscillations in Short Gamma-Ray Bursts, [Astrophys. J.](#) **983**, 88 (2025), arXiv:2408.16534 [astro-ph.HE].
- [32] S. Bernuzzi, D. Radice, C. D. Ott, L. F. Roberts, P. Moesta, and F. Galeazzi, How loud are neutron star mergers?, [Phys. Rev. D](#) **94**, 024023 (2016), arXiv:1512.06397 [gr-qc].

- [33] F. Zappa, S. Bernuzzi, D. Radice, A. Perego, and T. Dietrich, Gravitational-wave luminosity of binary neutron stars mergers, *Phys. Rev. Lett.* **120**, 111101 (2018), arXiv:1712.04267 [gr-qc].
- [34] J. M. Stone, P. D. Mullen, D. Fielding, P. Grete, M. Guo, P. Kempski, E. R. Most, C. J. White, and G. N. Wong, AthenaK: A Performance-Portable Version of the Athena++ AMR Framework, *arXiv e-prints*, arXiv:2409.16053 (2024), arXiv:2409.16053 [astro-ph.IM].
- [35] H. Zhu, J. Fields, F. Zappa, D. Radice, J. M. Stone, A. Rashti, W. Cook, S. Bernuzzi, and B. Daszuta, Performance-portable Numerical Relativity with AthenaK, *Astrophys. J. Suppl.* **278**, 50 (2025), arXiv:2409.10383 [gr-qc].
- [36] J. Fields, H. Zhu, D. Radice, J. M. Stone, W. Cook, S. Bernuzzi, and B. Daszuta, Performance-portable Binary Neutron Star Mergers with AthenaK, *Astrophys. J. Suppl.* **276**, 35 (2025), arXiv:2409.10384 [astro-ph.HE].
- [37] F. Banyuls, J. A. Font, J. M. A. Ibanez, J. M. A. Marti, and J. A. Miralles, Numerical 3+1 General Relativistic Hydrodynamics: A Local Characteristic Approach, *Astrophys. J.* **476**, 221 (1997).
- [38] L. Anton, O. Zanotti, J. A. Miralles, J. M. Marti, J. M. Ibanez, J. A. Font, and J. A. Pons, Numerical 3+1 general relativistic magnetohydrodynamics: A Local characteristic approach, *Astrophys. J.* **637**, 296 (2006), arXiv:astro-ph/0506063.
- [39] R. Borges, M. Carmona, B. Costa, and W. S. Don, An improved weighted essentially non-oscillatory scheme for hyperbolic conservation laws, *Journal of Computational Physics* **227**, 3191 (2008).
- [40] A. Harten, P. D. Lax, and B. v. Leer, On upstream differencing and godunov-type schemes for hyperbolic conservation laws, *SIAM Review* **25**, 35–61 (1983).
- [41] B. Einfeldt, C. Munz, P. Roe, and B. Sjögreen, On godunov-type methods near low densities, *Journal of Computational Physics* **92**, 273–295 (1991).
- [42] T. A. Gardiner and J. M. Stone, An Unsplit Godunov method for ideal MHD via constrained transport, *J. Comput. Phys.* **205**, 509 (2005), arXiv:astro-ph/0501557.
- [43] T. A. Gardiner and J. M. Stone, An Unsplit Godunov Method for Ideal MHD via Constrained Transport in Three Dimensions, *J. Comput. Phys.* **227**, 4123 (2008), arXiv:0712.2634 [astro-ph].
- [44] J. M. Stone, K. Tomida, C. J. White, and K. G. Felker, The Athena++ Adaptive Mesh Refinement Framework: Design and Magnetohydrodynamic Solvers, *Astrophys. J. Suppl.* **249**,

- 4 (2020), arXiv:2005.06651 [astro-ph.IM].
- [45] D. Hilditch, S. Bernuzzi, M. Thierfelder, Z. Cao, W. Tichy, and B. Bruegmann, Compact binary evolutions with the Z4c formulation, *Phys. Rev. D* **88**, 084057 (2013), arXiv:1212.2901 [gr-qc].
- [46] B. Daszuta, F. Zappa, W. Cook, D. Radice, S. Bernuzzi, and V. Morozova, GR-Athena++: Puncture Evolutions on Vertex-centered Oct-tree Adaptive Mesh Refinement, *Astrophys. J. Supp.* **257**, 25 (2021), arXiv:2101.08289 [gr-qc].
- [47] S. Gottlieb, C.-W. Shu, and E. Tadmor, Strong stability-preserving high-order time discretization methods, *SIAM Review* **43**, 89 (2001).
- [48] A. W. Steiner, M. Hempel, and T. Fischer, Core-collapse supernova equations of state based on neutron star observations, *Astrophys. J.* **774**, 17 (2013), arXiv:1207.2184 [astro-ph.SR].
- [49] A. Perego, S. Bernuzzi, and D. Radice, Thermodynamics conditions of matter in neutron star mergers, *Eur. Phys. J. A* **55**, 124 (2019), arXiv:1903.07898 [gr-qc].
- [50] P. L. Espino, P. Hammond, D. Radice, S. Bernuzzi, R. Gamba, F. Zappa, L. F. Longo Micchi, and A. Perego, Neutrino Trapping and Out-of-Equilibrium Effects in Binary Neutron-Star Merger Remnants, *Phys. Rev. Lett.* **132**, 211001 (2024), arXiv:2311.00031 [astro-ph.HE].
- [51] E. Gourgoulhon, P. Grandclement, K. Taniguchi, J.-A. Marck, and S. Bonazzola, Quasiequilibrium sequences of synchronized and irrotational binary neutron stars in general relativity: 1. Method and tests, *Phys. Rev. D* **63**, 064029 (2001), arXiv:gr-qc/0007028.
- [52] D. R. Lorimer, Binary and Millisecond Pulsars, *Living Reviews in Relativity* **11**, 8 (2008), arXiv:0811.0762 [astro-ph].
- [53] E. Gourgoulhon, *3+1 Formalism in General Relativity*, Vol. 846 (2012).
- [54] M. D. Duez, F. Foucart, L. E. Kidder, H. P. Pfeiffer, M. A. Scheel, and S. A. Teukolsky, Evolving black hole-neutron star binaries in general relativity using pseudospectral and finite difference methods, *Phys. Rev. D* **78**, 104015 (2008), arXiv:0809.0002 [gr-qc].
- [55] G. M. Webb, Q. Hu, B. Dasgupta, and G. P. Zank, Homotopy formulas for the magnetic vector potential and magnetic helicity: The Parker spiral interplanetary magnetic field and magnetic flux ropes, *Journal of Geophysical Research (Space Physics)* **115**, A10112 (2010).
- [56] V. Eswaran and S. B. Pope, An examination of forcing in direct numerical simulations of turbulence, *Computers and Fluids* **16**, 257 (1988).
- [57] J. R. Beattie, C. Federrath, N. Kriel, J. K. J. Hew, and A. Bhattacharjee, Taking control of

- compressible modes: bulk viscosity and the turbulent dynamo, *Mon. Not. Roy. Astron. Soc.* **542**, 2669 (2025), arXiv:2312.03984 [astro-ph.GA].
- [58] J. R. Beattie, C. Federrath, R. S. Klessen, S. Cielo, and A. Bhattacharjee, The spectrum of magnetized turbulence in the interstellar medium, *Nature Astronomy* **9**, 1195 (2025), arXiv:2504.07136 [astro-ph.GA].

SUPPLEMENTAL MATERIAL

1. Simulation Techniques

Both global and zoom-in simulations are performed using `AthenaK` [34–36]. Our code solves the equations of ideal general-relativistic magnetohydrodynamics in dynamical space-times [37, 38] using a 2nd order finite-volume approach. In particular, we use the 5th order `WENOZ` [39] scheme to reconstruct primitive variables to cell interfaces and the Harten–Lax–van Leer–Einfeldt (HLLE) approximate Riemann solver to compute numerical fluxes [40, 41]. The magnetic field is evolved using the upwind constrained transport scheme of Gardiner & Stone [42–44], which preserves the no-magnetic-monopoles constraint to machine precision. The background simulations evolve the spacetime metric using the Z4c formulation of Einstein equations [45], discretized using a 6th order finite differencing scheme, as described in detail in [35, 46]. In the zoom-in simulations, we evaluate the spacetime metric by interpolating the data from the background simulation, as discussed in detail below. We use a 3rd order, strong-stability preserving Runge–Kutta scheme for the time integration [47].

Neutron star matter is modeled using the finite-temperature, composition-dependent, SFHo equation of state [48]. Accordingly, matter inside the neutron stars is assumed to be composed of nucleons, electrons, and photons. Nuclear interactions are accounted for using a relativistic mean-field model. Nuclear statistical equilibrium is assumed at low densities. Our simulations do not explicitly include neutrino transport. However, we add neutrinos to the equation of state following the approach described in [49], which adequately captures the impact of neutrinos in the high-density, high-temperature regime relevant for our simulations [50].

2. Initial and Boundary Conditions

a. Global Simulations

We perform a simulation of an equal-mass binary NS merger. The initial data is generated with the `Lorene` pseudo-spectral code [51]. The initial configuration consists of two neutron stars with masses $m_1 = m_2 = 1.3 M_\odot$ at a separation of 45 km. The simulation domain consists of a box with sides of length 4535 km, with 192 points per dimension on the base

level, plus 8 additional nested refinement levels. We set the innermost level covering a box of size $\approx (74, 74, 30)$ km around the center of mass of the binary, so that the stars are completely contained during the full inspiral. The intermediate levels are automatically defined by the code provided the above parameters and the number of points per meshblock (see Ref. [34]), which we set to 32³.

On top of the hydrodynamic solution, we seed each of the neutron stars with a dipole-like field, defined through a vector potential which approximately describes the field generated by a current loop:

$$A_\phi = \frac{\pi r_0^2 I_0 \varpi^2}{(r_0^2 + r^2)^{3/2}} \left[1 + \frac{15r_0^2(r_0^2 + \varpi^2)}{8(r_0^2 + r^2)^2} \right], \quad (1)$$

where $\varpi^2 = (x - x_{\text{NS}})^2 + y^2$, $r^2 = \varpi^2 + z^2$, I_0 is the current, and r_0 is the radius of the current loop. We choose $r_0 \approx 3$ km and I_0 such that the maximum magnetic field, at the center of each star, is $B_{\text{max}} \approx 2 \times 10^{12}$ G. This choice provides a realistic magnetic field intensity at the surface of the stars [52]. The magnetic field extends outside the stars and fills the whole simulation domain.

We evolve the binary for ~ 7 orbits until the stars merge, and follow the post-merger for approximately 5 ms, covering the initial magnetic field amplification driven by the KHI. Figure 5 shows equatorial slices of mass density (ρ , left), temperature (T , center), and vertical magnetic field (B^z , right) at three different times for the global simulations.

b. Metric and Fluid Data

During the global simulation, we record simulation data in a cube of side length $2L$, $L = 4.5 GM_\odot/c^2 \simeq 6.65$ km centered about the origin. This data is used to provide initial data, boundary conditions, and background metric for the zoom-in simulations. To avoid possible boundary effects, the domain of the zoom-in simulations is restricted to a smaller cube with side length $2L'$, $L' = 4 GM_\odot/c^2 \simeq 5.91$ km. The data is stored on a Chebyshev endpoint grid with $N = 64$ points in each direction and sampled with a frequency of $\Delta t = 0.09375 GM_\odot/c^3 \simeq 0.46$ μ s. In particular, we store and interpolate the fluid baryon number density n_b , the Lorentz-factor-weighted three velocity $\tilde{v}^i = Wv^i$, W being the Lorentz factor, the pressure p , and the proton fraction Y_e of the plasma. The spacetime geometry is encoded in the lapse and shift vectors α and β^i , respectively, the three metric γ_{ik} , and the extrinsic curvature, K_{ik} . See, e.g., Ref. [53] for a definition of these

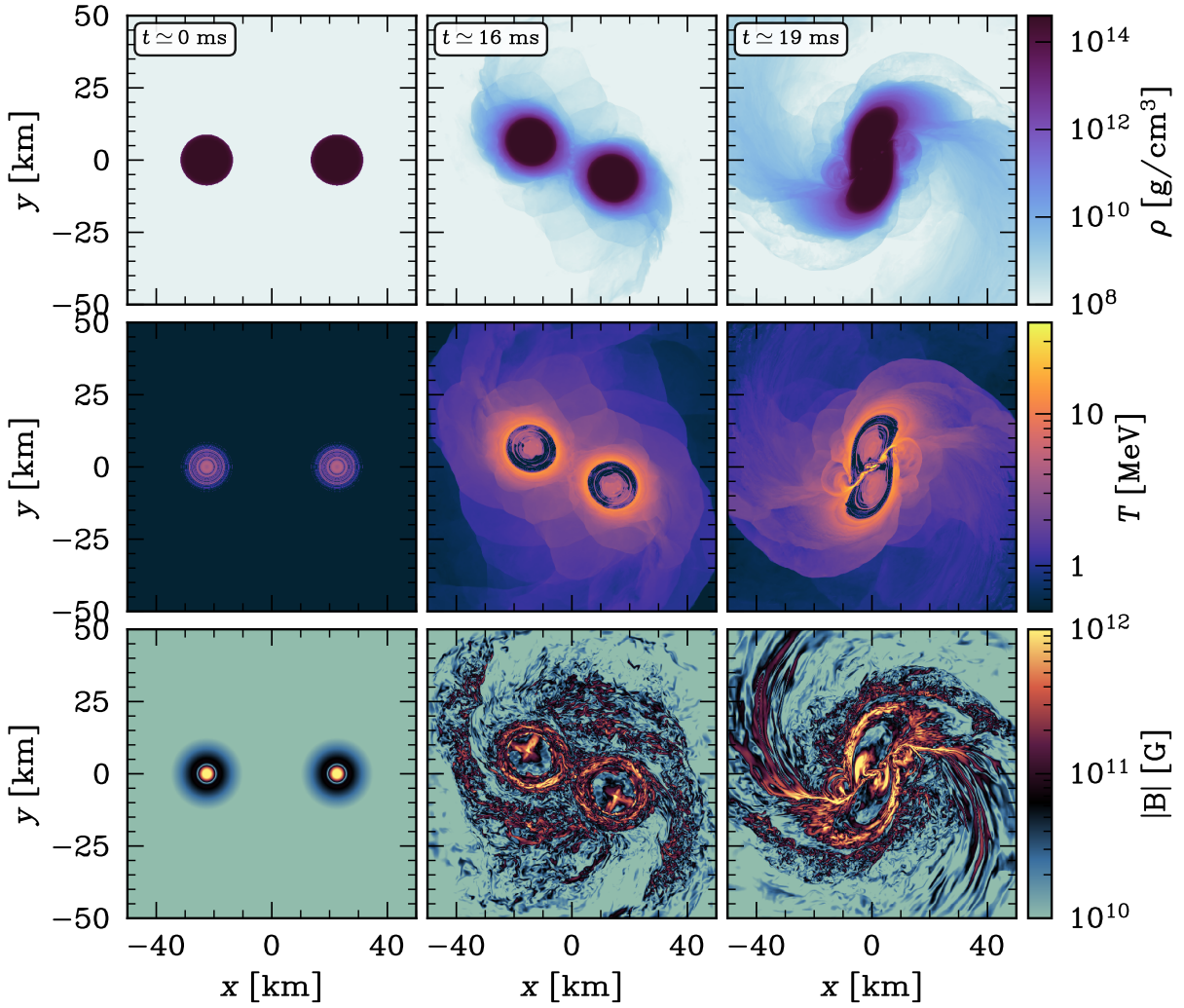


FIG. 5. **Equatorial slices of representative variables from the global simulation.** From top to bottom: Rest-mass density (ρ), temperature (T), and magnetic field strength($|\mathbf{B}|$). From left to right: $t \simeq 0, 16, 19$ ms.

quantities. Additionally, we store the Eulerian-frame densitized magnetic field $\mathcal{B}^i = \sqrt{\gamma} B^i$, γ being the determinant of the three-metric.

We interpolate all fields, except for the magnetic field (which is described in detail below), using 6th order Lagrange interpolation on the Chebyshev grid. This results in a speedup of a factor $\sim (N/5)^3 \simeq 2 \times 10^3$ compared to the direct evaluation of the Chebyshev collocation basis, which would have been prohibitively expensive, as we need to interpolate spacetime data and boundary conditions at each timestep of the zoom-in simulation. We have verified that the error introduced by this truncation of the interpolation stencil is negligible, as

can be expected since the weight associated with each collocation basis function decreases exponentially with distance from the collocation point for smooth data. This is the same approach used by `SpEC` to couple spacetime evolution, performed on spectral grids, and matter evolution, performed on a uniformly spaced grid [54].

c. Magnetic Field Interpolation

The interpolation of the magnetic field requires additional considerations to avoid the creation of magnetic monopoles. `AthenaK` applies boundary conditions using the standard “ghost cell” approach, whereby the domain is artificially extended by a few grid points on which data is prescribed. In the case of the zoom-in simulation, we prescribe data in this region by interpolation from the global simulation. To this aim, it is possible to directly interpolate the magnetic field. The reason is that, in the context of the upwind constrained transport, the ghost data is only used to compute the electric field at the cell edges. The magnetic field, which is collocated on the cell faces, is then updated using Faraday’s law, so its time derivative is divergence-free by construction. In other words, no divergence constraint violation can flow into the domain from the boundaries.

The initial conditions are more delicate, because the constraint-transport algorithm guarantees that the divergence of the magnetic field should stay constant to machine precision. Still, unphysical artifacts can be expected if the initial magnetic field is not solenoidal. As a first step, we reconstruct the vector potential using the identity [55]

$$\mathcal{A}_i(x) = \int_0^1 \epsilon_{ijk} \mathcal{B}^j(\lambda x) x^k \lambda d\lambda, \quad (2)$$

where ϵ_{ijk} is the antisymmetric symbol with $\epsilon_{123} = 1$. The integral in Eq. (2) is computed in pre-processing for each grid point using a Gaussian quadrature with 12 points. To this aim, the \mathcal{B} field data is interpolated to the quadrature points using a 10th order accurate Lagrange interpolation.

Next, we interpolate the vector potential \mathcal{A}_i at the cell edges of the zoom-in grid, using the same 6th order interpolation approach as for the other variables, and evaluate

$$\mathcal{B}^i = \epsilon^{ijk} \partial_j \mathcal{A}_k \quad (3)$$

using the discrete curl operator consistent with the constrained-transport of `AthenaK`, e.g.,

$$\mathcal{B}_{k,j,i+1/2}^1 = \frac{(\mathcal{A}_3)_{k,j+1/2,i+1/2} - (\mathcal{A}_3)_{k,j-1/2,i+1/2}}{\Delta x^2} - \frac{(\mathcal{A}_2)_{k+1/2,j,i+1/2} - (\mathcal{A}_2)_{k-1/2,j,i+1/2}}{\Delta x^3}, \quad (4)$$

where we have used the notation $f_{k,j,i}$ to denote the field at location $x^i = x_0^i + (i \Delta x^1, j \Delta x^2, k \Delta x^3)$.

3. Calculation of the Power Spectra

We compute power spectra for the density weighted three-velocity $\mathbf{w} = \sqrt{\rho} \mathbf{v}$ and for the Eulerian-frame magnetic field \mathbf{B} as

$$P_v(\mathbf{k}) = \frac{1}{2} \hat{\mathbf{w}}^* \cdot \mathbf{w}, \quad P_B(\mathbf{k}) = \hat{\mathbf{B}}^* \cdot \mathbf{B}, \quad (5)$$

where $\hat{\cdot}$ denotes the 3D Fourier transform and \cdot^* complex conjugation. Since we are not working in a periodic domain, we window the data using a symmetric Tukey window prior to the Fourier transformation. The Fourier transforms are computed in post-processing using the FFTW Python bindings.

One-dimensional spectra are defined as

$$P_v(k) = \int P_v(\mathbf{k}) \delta(|\mathbf{k}| - k) d^3\mathbf{k}, \quad (6)$$

where δ is the Dirac delta. The one-dimensional magnetic field spectrum is defined in an analogous way. Note that, since we are working in a finite domain, the spectra are quantized, so all integrals reduce to summations. Integrals over spherical shells are transformed to weighted sums following [56]:

$$P_v(k) = \frac{4\pi k^2}{N_k} \sum_{k-1/2 < |\mathbf{k}| \leq k+1/2} P_v(\mathbf{k}), \quad (7)$$

where N_k is the number of discrete wave-numbers in the shell $k - 1/2 < |\mathbf{k}| \leq k + 1/2$.

4. Magnetic field evolution

In this Section, we provide additional diagnostics and analysis of the magnetic field evolution in our simulations. The exponential amplification of the field seen in our simulations is consistent with the action of a small-scale dynamo driven by turbulence. Similar amplification mechanisms operate in other turbulent astrophysical environments such as the interstellar medium (e.g., Beattie et al. [57, 58]). In Figure 6, we show 2D snapshots of the magnetic field evolution at several times from the beginning of the simulation until the end. The initially smooth shear layer rapidly develops vortical structures due to the KHI.

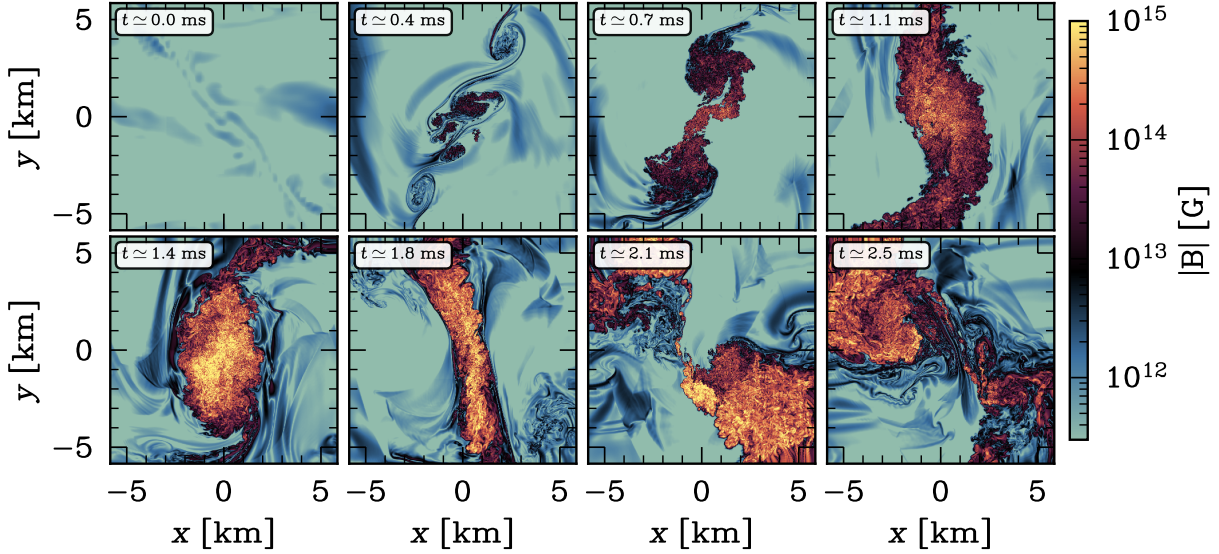


FIG. 6. Evolution of the shear layer and magnetic field. Equatorial slices of the magnetic-field strength at selected times for the $\Delta x \simeq 2.9$ m simulation, showing the development of Kelvin–Helmholtz-driven turbulence.

Several large vortices form along the layer, which in turn become themselves KH-unstable and become turbulent approximately after one turnover time; the magnetic field lines are stretched, twisted, and folded within these regions and are exponentially amplified. As time passes, the initial vortices merge into larger ones and ultimately coalesce into a single, thick turbulent layer. The magnetic field continues to be amplified at small scales due to the turbulence until approximately 2 ms. The process continues with the turbulent layer separating again into 2 or more coherent structures with large magnetic fields due to the nonlinear global dynamics.

Turbulence driven by the KHI leads to the formation of small, intermittent current sheets embedded within the turbulent cascade. These structures arise from the accumulation of vortices across a range of scales and the onset of secondary instabilities. Because the current density $\mathbf{j} \approx (c/4\pi) \nabla \times \mathbf{B}$ directly traces magnetic-field gradients, it provides a particularly clear diagnostic of regions where the field is strongly stretched, twisted, and folded by the flow, and where magnetic tension, pressure forces, and reconnection become dynamically important. Regions of enhanced current, therefore, highlight locations where small-scale kinetic energy is efficiently transferred into magnetic energy. In Fig. 7, we show the component of the current density perpendicular to the equatorial plane at $t \simeq 1.5$ ms; it demonstrates

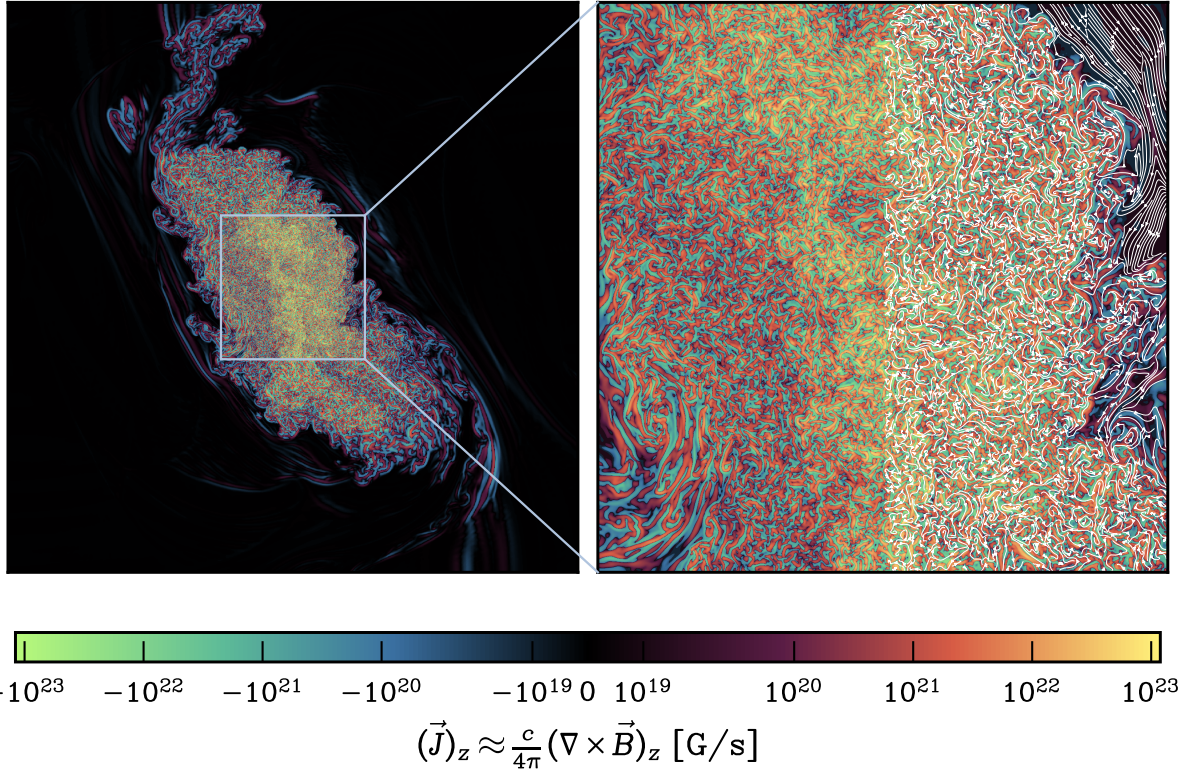


FIG. 7. **Intermittent current-sheet formation.** Equatorial snapshot of the vertical component of the (Newtonian) current density $\mathbf{j} = (c/4\pi) \nabla \times \mathbf{B}$ at $t \simeq 1.5$ ms. The right panel shows a zoomed-in region of size ≈ 3 km; magnetic field lines are superimposed on the right half of the plot, tracing the intermittent current sheet structures.

how the small-scale current sheets permeate the full volume of the turbulent region.

The intermittency of magnetic-field amplification in small-scale turbulent eddies can be quantified using the cumulative volume distribution for the magnetic field strength, $p(B > B_0)$, defined as the fraction of the volume within which the magnetic field exceeds a certain value B_0 . In other words, this measures the propensity of a given region of the plasma to have a magnetic field amplified to a given strength. In Figure 8, we show the time evolution of this quantity for all our simulations at different numerical resolutions. At early times, the magnetic field is weak throughout most of the volume, with the bulk of the domain having $B \lesssim 10^{11}$ G and only a small portion reaching field strengths above 10^{12} G. Once the magnetic amplification sets in, all simulations rapidly develop exponential tails with high- B in the cumulative distribution. As expected, the extent of this tail is strongly resolution dependent: higher-resolution runs populate more regions with progressively higher

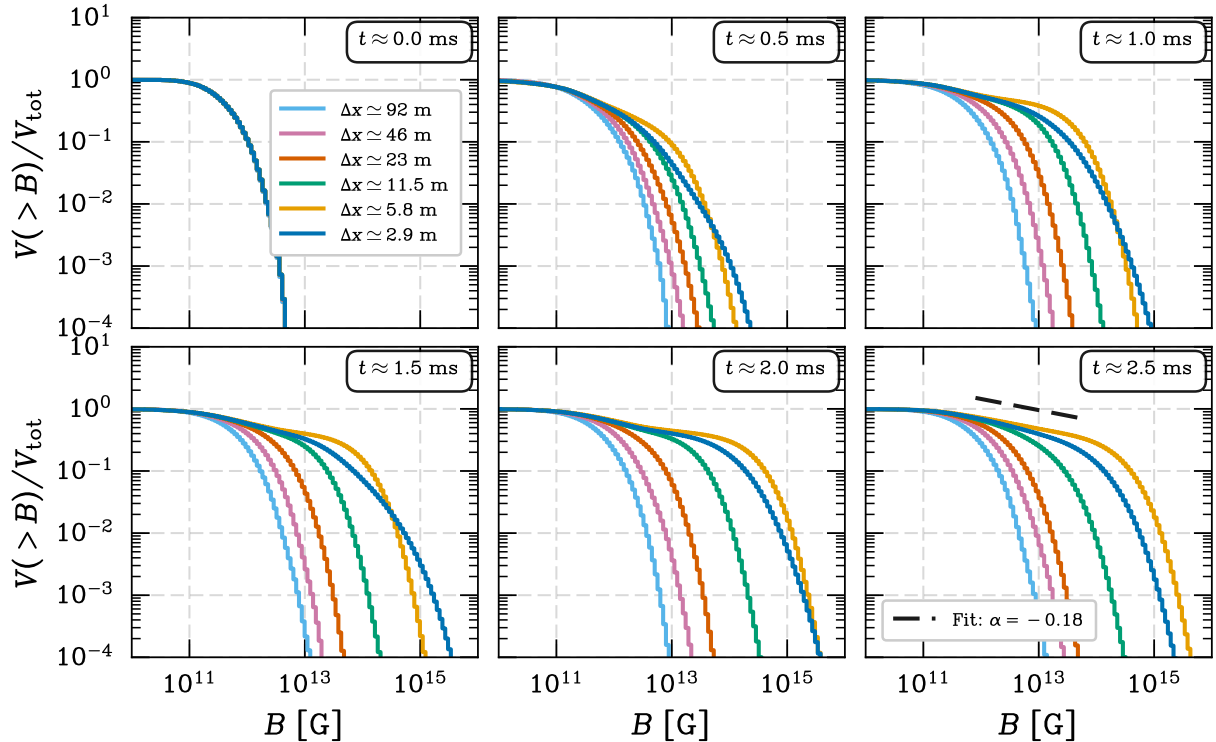


FIG. 8. **Cumulative volume distribution of magnetic-field strength.** Cumulative volume fraction, $p(B > B_0)$, at different times for all simulations. In the final panel, a power-law fit (short dashed line) is shown for the unigrid $\Delta x \simeq 5.8$ m simulation.

magnetic-field strengths. By $t \sim 1$ ms, the two highest-resolution simulations already exhibit a non-negligible portion of the domain with fields $> 5 \times 10^{14}$ G.

The shape of the exponential tail depends on the simulation setup. In particular, our highest-resolution run employs a mesh-refinement strategy where only a fraction of the volume attains the maximum resolution, while a substantial portion has approximately half the resolution of the unigrid simulation with $N = 2048^3$ ($\Delta x \simeq 5.8$ m). As a result, at times > 1.5 ms, this run exhibits a shallower tail, with fewer regions at $B \sim 10^{14}$ G, but extending to higher field strengths than the unigrid $N = 2048^3$ case. By the end of the runs, both high-resolution simulations have developed a distinct power-law tail at magnetic-field strengths below those of the exponential tail; this feature is not clearly visible in the lower-resolution runs. From $t \simeq 2$ ms until the end of the simulations, the cumulative distribution follows a power-law $p(B > B_0) \sim B_0^{-p}$, with $p \approx 0.18$. The emergence of such power-law tails is consistent with strongly intermittent magnetic-field amplification driven by the KHI-induced

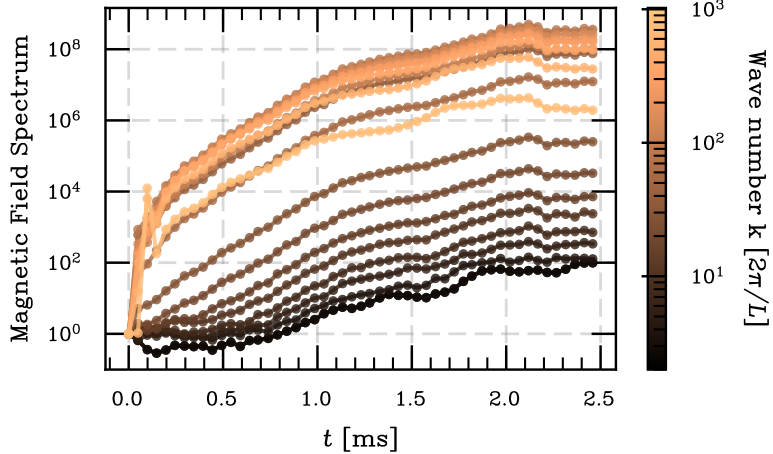


FIG. 9. **Time-evolution of the magnetic-field power spectrum at individual wavenumbers.** Magnetic-field power as a function of time for individual wavenumbers k in the $\Delta x \simeq 5.8$ m simulation.

turbulence.

In Figure 9, we show the time-evolution of the magnetic-field power spectrum, resolved into individual Fourier modes $k = 0, \dots, 1024$. Early in the run, magnetic energy grows exponentially at high wavenumbers, corresponding to small spatial scales, while power at larger scales remains nearly unchanged. This behavior reflects the initial amplification of the field by small-scale turbulence associated with the KHI. As the simulation proceeds, power at progressively lower wavenumbers begins to increase, after the small-scale field has reached sufficiently large amplitudes. Such a delayed growth of the larger-scale modes is consistent with a net transfer of magnetic energy from small to large scales by an inverse cascade or nonlinear processes. Likely, the amplified small-scale twisted field gives rise to reconnection where the magnetic energy reorganizes on larger scales. Importantly, this behavior is absent in the low-resolution runs; this supports the interpretation that the growth of large-scale magnetic fields is a secondary, nonlinear process driven by small-scale magnetic amplification and not due to some large-scale dynamical effect.

Finally, in Figure 10 we show the kinetic and magnetic energy spectra at the final time for all simulations. The magnetic field does not reach equipartition with the kinetic energy, staying subdominant by approximately three orders of magnitude. Because the amplification proceeds entirely in the kinematic regime, a higher initial magnetic field in the neutron stars

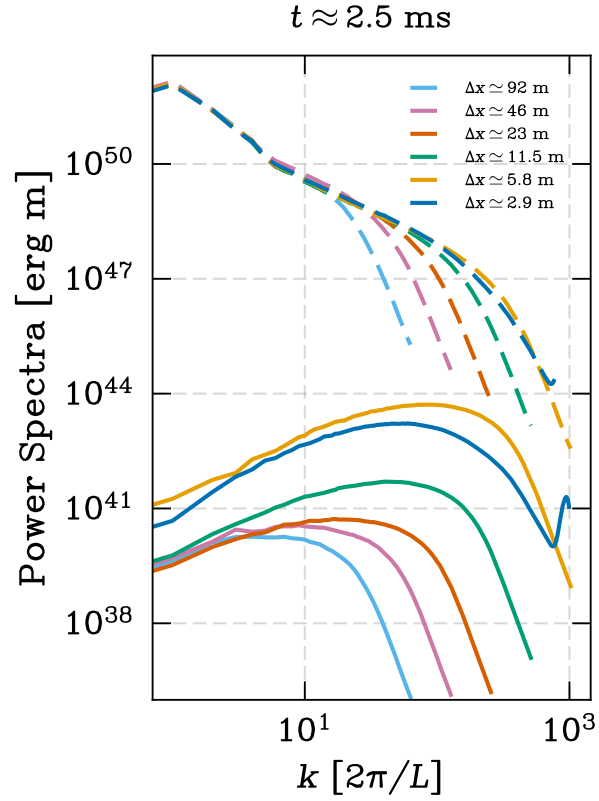


FIG. 10. **Kinetic and magnetic power spectra at different numerical resolutions.** Dashed lines show kinetic spectra; solid lines show magnetic spectra.

would likely allow the system to approach equipartition by the end of the simulation.